Rendon-Patiño, A.; Torres-Martí, F.; Primo Arnau, AM.; García Gómez, H. (2022). Band gap alignment of structured microporous graphitic carbons by N doping and its influence on photocatalytic overall water splitting. Sustainable Energy & Fuels. 6(9):2170-2178. https://doi.org/10.1039/D2SE00078D

# Band gap alignment of structured microporous graphitic carbons by N doping and its influence on the photocatalytic overall water splitting

Alejandra Rendón-Patiño[a], Ferran Torres[a], Ana Primo[a,*] and Hermenegildo García[a,*]

[a] Instituto de Tecnología Química, Consejo Superior de Investigaciones Científicas-Universitat Politecnica de Valencia, Universitat Politécnica de Valencia, Av. De los Naranjos s/n, 46022 Valencia, Spain.

**ABSTRACT**

Hydrogen generation from water using solar light could be a process of paramount importance in the forthcoming decarbonized society. This reaction requires of efficient photocatalysts based on earth-abundant elements. Metal-free carbon semiconducting materials are very appealing in this regard. This manuscript shows that N-doping is a convenient strategy to increase the photocatalytic activity of microporous graphitic carbons obtained from pyrolysis of $\alpha$–, $\beta$– and $\gamma$–cyclodextrins. These (N)C carbons exhibit enhanced photocatalytic activity for $H_2$ generation in the presence of methanol respect to undoped analogs. The optimal (N)C material (pore size, 0.65 nm) was the one derived from $\alpha$–cyclodextrin at N content of 3.1 %, achieving at 4 h a $H_2$ productivity of 1.8 mmol$\times g^{-1}$ in the presence of methanol. These materials also exhibit photocatalytic activity for overall water splitting, although with lesser efficiency than $H_2$ generation in the presence of sacrificial electron donors. The present results illustrate the tuning of band alignment by N-doping in the graphitic matrix.

*Keywords:* Photocatalysis, water splitting, carbocatalysis, hydrogen production

*Corresponding authors. Tel: 34 96387 7807. E-mails: aprimoar@itq.upv.es (Ana Primo) and hgarcia@upv.es (Hermenegildo Garcia)

## 1. Introduction

Pyrolysis of oligo- and polysaccharides forms graphitic carbons that often can be exfoliated by sonication into single or few layers defective graphenes.[1-3] In this regard, we recently reported the uniqueness of cyclodextrin pyrolysis, since these organic capsules form particulate graphitic carbon residues with (ultra)micropores of uniform subnanometric dimensions.[4, 5] Cyclodextrins are cyclic molecular oligomers of 1,4-glucopyranose with a rigid geometry of truncated cones of 0.79 nm height.[6-9] The diameter of the cone is a function of the number of glucose units ranging for external larger diameter from 1.37 to 1.69 nm for $\alpha-$ and $\gamma$-cyclodextrins, respectively.[10] It has been proposed that, upon melting at temperatures about 300 $^{o}$C, these cyclic molecules undergo spontaneous self-assembly forming tubes.[5] Subsequent chemical transformation of self-assembled cyclodextrin melts into the graphitic carbon residue retains the regular micropore structure, resulting in a highly crystalline graphitized porous carbon.

Porosity plays an important role in adsorption and catalysis.[11, 12] When the dimensions of the pores are commensurate with the molecular size of substrates, remarkable effects derived from the strong non-covalent interaction of reagents and substrates with the walls of porous materials resulting from the tight fit, can arise.[13, 14] One clear example is Brönsted acidity of zeolites that is much stronger than expected due to the operation of confinement effects, this being reflected in a much higher proteolytic activity of zeolites in catalytic cracking of hydrocarbons compared to non-porous aluminosilicates.[14, 15] Similarly, it could be expected that defective graphitic carbons acting as metal-free catalysts could exhibit an increased activity when these carbons are structured as microporous solids with pore dimensions in the range of the molecular size of substrates and reagents.

Another reaction type that has been reported for defective doped graphenes, derived from their semiconducting property, is the photocatalytic overall water splitting.[4] In the case of exfoliated defective graphenes, it has been observed that N-doping introduces photocatalytic activity for $H_2$ generation in the presence of electron donors.[16] Although much less documented than for thermal catalytic reactions, it can also be expected that microporosity can play a role increasing the photocatalytic activity as consequence of the confinement of the substrates and reaction intermediates. Thus, the combination of doping and porosity could be an effective way to obtain advanced carbon-based semiconductors with improved performance.[5]

In view of the above comments, it would be of interest to determine the effect of N-doping on the conduction and valence band energy values of semiconducting microporous graphitic carbons and their influence on their photocatalytic activity. By controlling the amount and distribution of N atoms, tuning of the edge energy of the conduction and valence band could be possible and this should be reflected on the photocatalytic activity of these porous carbons. Herein, it will be disclosed how N-doping of graphitic carbons derived from cyclodextrins [(N)C] with regular microporosity modifies the position of the conduction and valence band, influencing the photocatalytic activity of these materials that are able to promote even the photocatalytic overall $H_2O$ splitting in the absence of sacrificial agents.

## 2. Experimental section

### *2.1. Synthesis of (N)C*

200 mg of α-cyclodextrin (0.41 mmol, 972.8 g/mol, Sigma-Aldrich) were dissolved in 20 mL of MilliQ water. Various amounts of a urea solution (60 mg/mL, Sigma-Aldrich) were added under constant stirring to obtain 10, 50 and 300 wt% of nitrogen respect to the cyclodextrin (0.25 mL,

1.22 mL, 7.45 mL for (N)$C_\alpha$-1, (N)$C_\alpha$-2 and (N)$C_\alpha$-3 respectively). After 24 h of stirring, the water was removed by heating the solution in a silicone bath at 60 $^oC$.

Pyrolysis of (N)C was performed in a horizontal electric oven and using the following heating program: 10 $^oC$ / min up to 900 $^oC$ for 2 h. The graphenic material was milled before characterization and photocatalytic tests.

For β-cyclodextrin (0.352 mmol, 1135 g/mol, Sigma-Aldrich) and γ-cyclodextrin (0.308 mmol, 1297.12 g/mol, Sigma-Aldrich) an identical preparation procedure as that described for (N)$C_\alpha$ was followed.

*2.2. Photocatalytic tests*

All the photocatalytic tests were performed using a 51 mL volume cylindrical quartz photoreactor and was irradiated using a 300 W Xe lamp (Hamamatsu, 1.6 sun power) or simulated sunlight irradiation (OrielTM, 0.8 sun power). For overall water splitting, the photocatalyst was dispersed in 30 mL of ultrapure water (1.5 mg/mL) with a sonicator. For hydrogen evolution tests, 10 mg of catalyst was dispersed in 20 mL of methanol solution (20 % w/v) or triethanolamine solution (20% w/v). Then, it was introduced in the reactor and the atmosphere was purged with an argon flow for 15 min. For oxygen evolution tests, 10 mg of catalyst with $CrO_2$ was dispersed in Ag aqueous solution (0.1 mM). The evolved $H_2$ and $O_2$ were analyzed by using a gas chromatograph (Agilent 490 MicroGC) equipped with a molecular sieve of 5 Å column with TC detector and Ar as the carrier gas.

*2.3. Photodeposition of Pt*

20 mg of catalyst was dispersed in 16 mL of 0.1 mM $H_2PtCl_4$ solution by sonication, and then 4 mL of methanol was added to the dispersion as electron donor. The aqueous solution was purged

with Ar and was irradiated using a 300 W Xe lamp. Then, the black solid was collected by centrifugation and was washed several times with Milli-Q water. This material was used for the hydrogen evolution test and characterized by HRTEM and EDX.

*2.4. Photodeposition of $CrO_2$*

20 mg of the catalyst was dispersed in 20 mL of $CrCl_2$ solution (0.1 mM) by sonication and subsequently the photoreactor was filled with oxygen (1 bar) as the electron scavenger. Afterwards, the dispersion was irradiated at 25 $^oC$ with Xe lamp for 15 min and thoroughly washed with MilliQ water. The formation of $CrO_2$ were confirmed by HRTEM and EDX.

*2.5. Photoelectrochemical test*

Photoelectrochemical measurements were made in a conventional three electrode electrochemical cell using Ag/AgCl disc as pseudo-reference electrode and Pt wire auxiliary electrode that accompanies the N-doped graphene deposited as a film on Fluorine doped Tin Oxide (FTO) glass as working electrode. Voltammetric measurements were carried out with a potentiostatic device Solartron, using KCl 1.0 M saturated with $N_2$ as electrolyte. The working electrodes were the (N)$C_\alpha$-2 with 1 % of Paraloid that were deposited on FTO.

*2.6. Physicochemical characterization*

Raman spectra were recorded with a 514 nm laser excitation on a Renishaw Raman spectrometer ("Reflex") equipped with a Leica optical microscopy and a charged coupled device camera. The laser power in the sample was 25 mW. Each spectrum was the average of 20 acquisitions. TEM images were recorded on a JEOL JEM 2100F with an acceleration voltage of 200 kV coupled with X-Max dispersive energy X-ray detector (EDX). X-ray photoelectron spectroscopy (XPS) measurements were carried out in a SPECS instrument, which included an XPS spectrometer

equipped with a monochromatic X-ray source Al Kα1 (photonic energy 1486.74 eV), operating under ultrahigh vacuum at $1.3 \times 10^{-13}$ atm. The binding energies were corrected for surface charge effects during measurements using the central level of C1s (284.5 eV) as internal reference. The elemental analysis (EA) were carried out with a Euro EA 3000. Thermogravimetric analysis were performed using a Mettler Toledo TGA/SDTA 851 station in the temperature range of 25 $^{o}$C- 900 $^{o}$C with a scanning speed of 10 $^{o}$C $min^{-1}$ and a $N_2$ flow of 30 mL $min^{-1}$. XRD pattern was recorded using a Cubix-pro PANalytical diffractometer.

## 3. Results and discussion

### *3.1. Characterization of (N)C samples*

Considering the ability of cyclodextrins to form inclusion complexes,[6] N-doping was simply accomplished by mechanical mixing urea as N source and cyclodextrins, followed by subsequent pyrolysis in an electrical oven under Ar atmosphere at 900 $^{o}$C. Three (N)C samples with different N content from 4.7 to 13.7 % were initially prepared and characterized. It should be noted that besides N, the presence of residual O from the original cyclodextrin composition is also present, although its percentage, around 9 wt.%, is similar for the three samples. Besides $\alpha$-cyclodextrin, two additional (N)C samples using $\beta$ and $\gamma$-cyclodextrin were prepared at the intermediate urea content. The (N)C samples under study and their analytical data are summarized in Table 1.

Table 1. Analytical data of graphitic carbon residues obtained by pyrolysis of α-, β-, and γ- cyclodextrins with urea.

| Sample | C (%) [a] | N (%) [a] | Surface area ($m^2/g$) | Band gap (eV) |
|---|---|---|---|---|
| **(N)$C_\alpha$-1** | 85.7 | 4.2 | 547 [b] | 1.9 |
| **(N)$C_\alpha$-2** | 84.3 | 6.7 | 540 [b] | 2.0 |
| **(N)$C_\alpha$-3** | 75.2 | 13.7 | 490 [b] | 2.1 |
| **(N)$C_\beta$** | 84.1 | 3.9 | 558 [b] | 2.2 |
| **(N)$C_\gamma$** | 86.7 | 2.4 | 434 [c] | 2.4 |

[a] It is assumed that the rest to 100 % is residual oxygen. [b] Measured by $CO_2$ adsorption. [c] Measured by $N_2$ adsorption

The values of specific BET surface area are provided in Table 1 (see also Figure S1 in Supporting information). Only sample (N)$C_\gamma$ exhibits $N_2$ adsorption, giving a BET specific surface area of 434 $m^2/g$ (see footnote c in Table 1). The other four (N)C samples did not adsorb $N_2$, a fact that can be attributed to the small pore size. In contrast, the internal surface area of these four samples could be measured by $CO_2$ adsorption, giving similar specific surface area about 500 $m^2/g$. These BET surface area values are comparable to other microporous materials, such as zeolites.

Thermogravimetric analysis indicates that the (N)$C_\alpha$ are thermally stable in air up to 500 $^oC$, undergoing a complete combustion in the range from 500 to 700 $^oC$ (see Figure S.2-S.6 in supporting information). However, there was a shift on the temperature of calorimetric peak from 590 to 630 $^oC$ as the N content increases, reflecting a higher thermal stability as a function of the N content in the (N)$C_\alpha$. In comparison to (N)$C_\alpha$ at similar N doping level, the temperature of maximal heat evolution for (N)$C_\beta$ and (N)$C_\gamma$ samples are somewhat lower, about 590 $^oC$.

The defective graphitic nature of the (N)C carbons was assessed by Raman spectroscopy. Three characteristic peaks at 2850 (broad), 1590 and 1350 $cm^{-1}$ corresponding to the 2D, G and D

bands in defective graphenes were recorded with minor variation among the samples (Fig. S.7 in Supporting information). The intensity of the G vs. the D band can be taken as a quantitative indicator of the density of defects of the graphene sheets.[17] For the present (N)C samples the $I_G/I_D$ ratio was between 1.1 and 1.2 that is in the range, or even somewhat higher, of values commonly observed for defective N-doped graphitic materials derived from saccharide pyrolysis.[3]

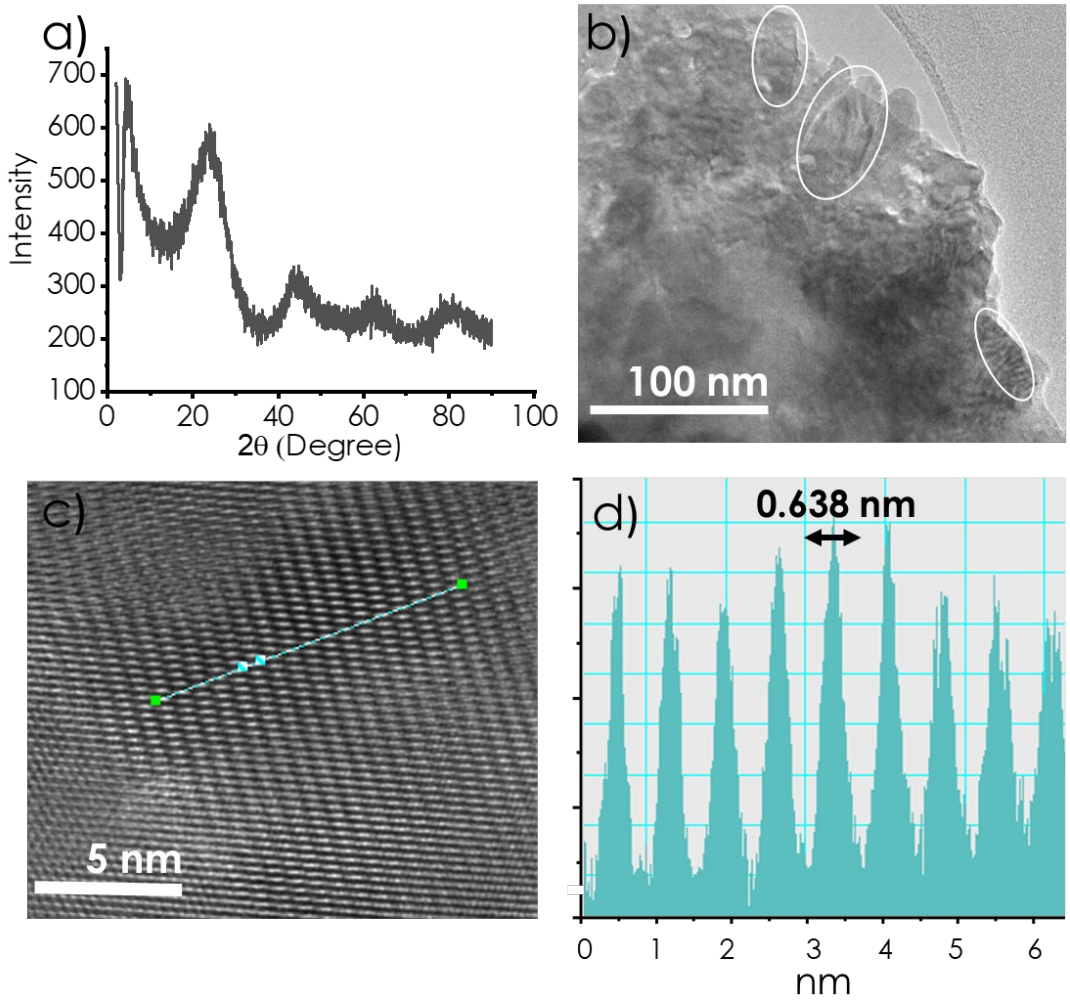


**Fig. 1.** a) XRD spectra and b), c) and d) High resolution TEM images showing the channel structure and the dimensions of the corresponding channels of (N)C$_\alpha$-2.

XRD of the (N)$G_{CD}$ samples are similar, exhibiting peaks at angle values of 24, 45 and 62 º (Figure 1). These diffraction peaks are typical for graphitic carbon and can be indexed as corresponding to the diffraction in the 002, 101 and 004 planes.[18]11 In the present case of (N)C, the large peak width

This indicates their small particle size and/or the lower carbon crystallinity compared to graphite. Worth noting is the presence of an additional diffraction peak at short angles between 4 and 12 º that can be associated to the presence of regular channels in these materials (see Figure 1 and Figure S8 in Supporting information)

The remarkable crystallinity and porosity of the graphitic structure indicated in XRD can be observed in the TEM images of the samples. As an example, Fig. 1 shows a TEM image of the particulate (N)$C_\alpha$-2 showing that the carbon residue is constituted by irregular particles of about 20-30 nm dimensions. In aqueous suspension, measurements by dynamic laser scattering show a uniform particle size of 100 nm, with a remarkable stability in accordance with the high negative zeta potential value of – 46.2 mV (Figure S9 in supporting information). High-resolution TEM shows the presence of channels. Measurement of the periodic contrast variation in certain parts of the image show a strictly regular pore dimension of 0.64, 0.74 and 0.78 nm for (N)$C_\alpha$, (N)$C_\beta$ and (N)$C_\gamma$, respectively. Figure S10 in Supporting information shows similar images for the set of samples under study.

Survey XPS analysis of the (N)$C_\alpha$ samples reveals the presence of C, N and O. Quantification of the N/C atomic ratio by XPS coincides well with combustion chemical analysis. Experimental C1s peak can be adequately deconvoluted to three components corresponding to graphitic carbon (284.8 eV), C bonded to N or O with single (286.2 eV) and C atoms of carboxylic acid groups (289.5 eV). Figure 2a presents an illustrative example showing the experimental C1s peak and its best fitting

to three components. As expected, while the proportion of the graphitic C atoms decreases from 39.7 to 29.3 % with the increase of N atoms, the proportion of C atoms bonded to N grows accordingly from 47.7 to 52.8 % (see Figure 2). In accordance the total percentage of surface N atoms increases gradually from 2.15 to 5.36 % going from (N)$C_\alpha$-1 to (N)$C_\alpha$-3.

Analysis of the XPS N1s peak of the (N)$C_\alpha$ samples show the presence of two components corresponding to pyridinic (398.3 eV) and graphitic (401.5 eV). Fig. 2 shows the XPS N1s peaks and their best fit to two components. Importantly, both types of N atoms grow with the total N atoms, indicating that the increase in N doping does not change their relative distribution.

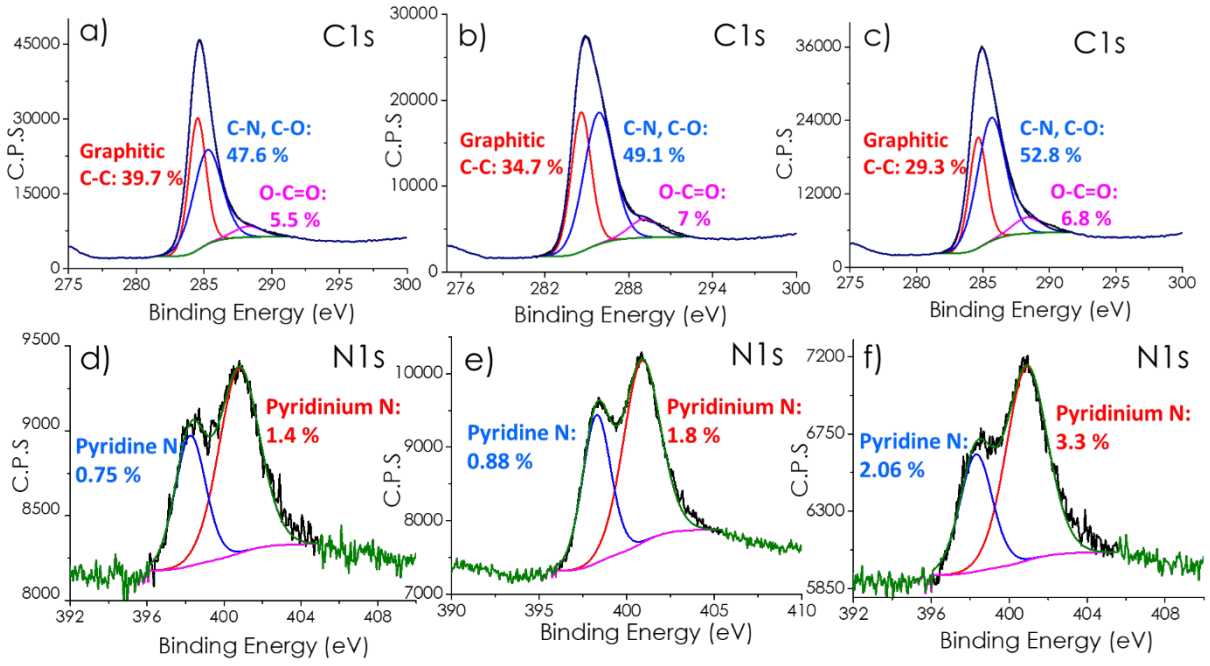


**Fig. 2.** Deconvoluted C1s XPS of a) (N)$C_\alpha$-1 b) (N)$C_\alpha$-2 c) (N)$C_\alpha$-3 and N1s XPS of d) (N)$C_\alpha$-1 e) (N)$C_\alpha$-2 f) (N)$C_\alpha$-3.

*3.2. Photocatalytic activity.*

All the samples were screened for their ability to promote $H_2$ generation upon UV-Vis, simulated sunlight or visible light illumination. Irradiations were carried out upon dispersing the (N)C samples in 3:1 $H_2O$/methanol under continuous magnetic stirring at room temperature. All the (N)C samples promoted the formation of $H_2$ in different amounts depending on the material and conditions.

Initial measurements were aimed at finding the optimal amount of solid upon UV-Vis irradiation in methanol at room temperature. It is a general behavior that depending on the light intensity, reactor geometry and other experimental conditions there is an optimal amount of photocatalyst to achieve the highest $H_2$ production. Lower photocatalyst amounts result in lesser photons being absorbed, while larger photocatalyst amounts decrease light penetration into the photoreactor by reflection and scattering and it may result also in lesser $H_2$ generation. In our case, it was found that 0.1 $g \times L^{-1}$ was the concentration of (N)$C_\alpha$-2 with the highest $H_2$ evolution, reaching a value of 1.8 $mmol \times g^{-1}$ in 4 h irradiation. The results are presented in Fig. 3. This productivity value is quite remarkable, considering that this is a metal-free photocatalyst. Table S1 in the Supporting information compares the photocatalytic performance of (N)$C_\alpha$-2 with other related N-doped carbons reported in the literature. Although these comparisons have to be taken cautiously due to differences in operating systems and conditions, it shows that the photocatalytic activity of (N)$C_\alpha$-2 is among the highest achieved for N-doped carbon materials, although lower than that of graphitic carbon nitride doped with 1 wt.% Pt.

Interestingly in the case of (N)$C_\alpha$-2, the temporal profile of $H_2$ evolution exhibits an induction period in all the plots. It is proposed that during this induction period, the gases evolved become

adsorbed onto the (N)$C_\alpha$-2 until the solid becomes saturated and the presence of $H_2$ can be detected in the head space.

The influence of the N-doping was addressed also in the presence of methanol by comparing the temporal profiles of $H_2$ evolution of the three (N)$C_\alpha$ samples with that of the undoped $C_\alpha$ under the same conditions. It was found that the presence of N atoms as dopant increases the catalytic activity of these graphitic carbons, there being a maximum for (N)$C_\alpha$-2, whose catalytic activity increases by a factor of three with respect to the $H_2$ production of the undoped $C_\alpha$ material. The results are presented in Figure 3 b. This indicates the benefits of doping. However, if the density of N atoms is too high, the catalytic activity decreases, probably due as a favored electron-hole recombination as it happens with other semiconductors.

The next parameter to be studied was the influence of the pore size and, therefore, the number of glucose units in the cyclodextrin precursor. For (N)C samples at the same N-doping level, it was observed that the material derived from $\alpha$–cyclodextrin is the one exhibiting the highest photocatalytic efficiency, while the performance of (N)C derived from $\beta$- and $\gamma$–cyclodextrins is almost coincident. Figure 3 c presents the temporal $H_2$ evolution profiles for the (N)C samples as a function of the cyclodextrin precursor.

Stability of (N)$C_\alpha$-2 photocatalyst was assessed by performing four consecutive uses of the same sample at 40 $^oC$ following the temporal profile of $H_2$ evolution. The results are presented in Figure 3 d. A gradual decay in photocatalytic activity for the third and fourth use going from 680 to 640 and 600 $\mu$mol $H_2 \times g^{-1}$ was observed.

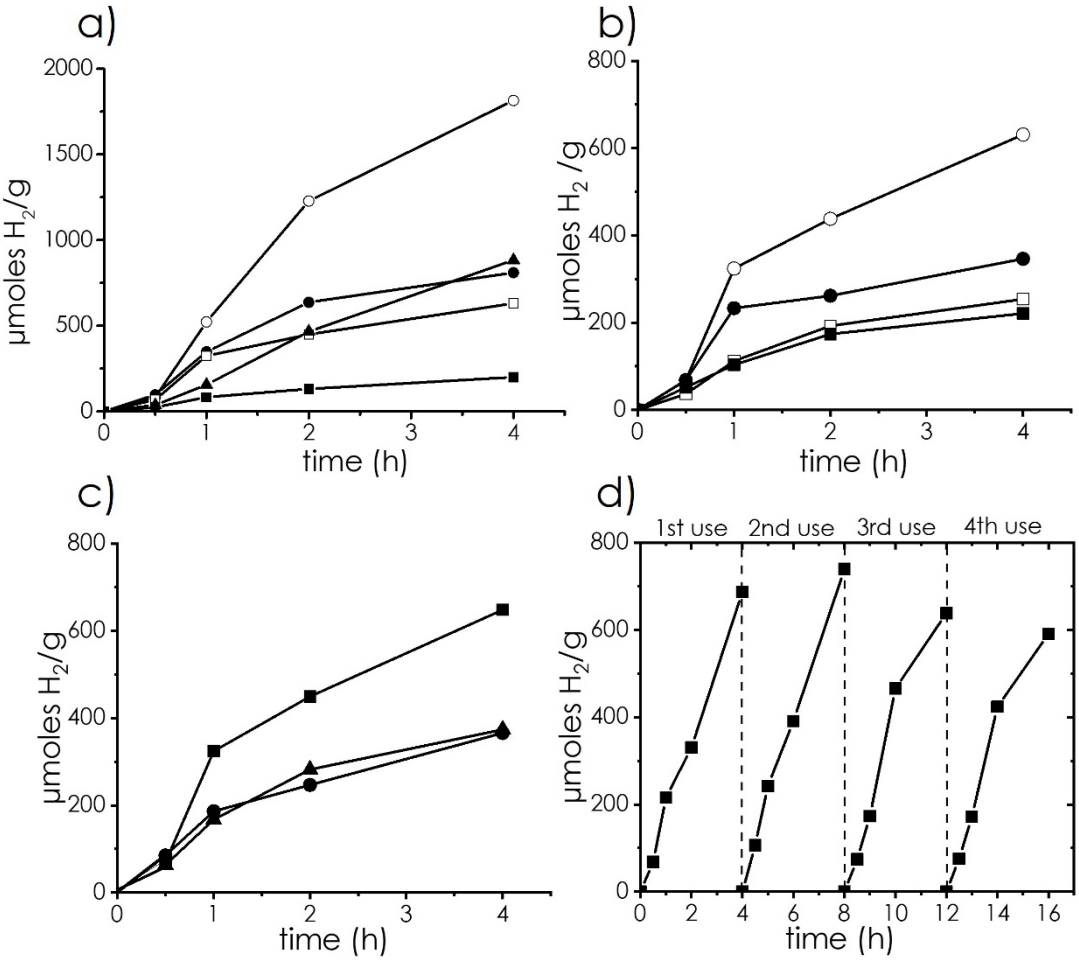


**Fig. 3.** Temporal profiles of hydrogen evolution using a) different concentrations of (N)$C_\alpha$-2: ▲ 0.05 g× $L^{-1}$,❍ 0.1 g×$L^{-1}$, ● 0.25 g×$L^{-1}$, □ 0.5 g×$L^{-1}$ and ■ 1.0 g×$L^{-1}$; b) different % N-doping of (N)$C_\alpha$: ❍ (N)$C_\alpha$-2, ● (N)$C_\alpha$-3, □ (N)$C_\alpha$-1 and ■ $C_\alpha$; c) different precursors of cyclodextrins: ■ (N)$C_\alpha$-2, ▲ (N)$C_\beta$ and ● (N)$C_\gamma$. and d) reuses of (N)$C_\alpha$-2. Reaction conditions: 0.5 g×$L^{-1}$ of (N)C, Milli-Q water 20 mL with methanol (20 v/v %) as electron donor, photoreactor volume 51 mL, UV−vis irradiation by a 300 W Xe lamp, ambient temperature.

The influence of the temperature and the nature of electron donor was analyzed by performing a comparison of the temporal profiles of $H_2$ evolution at different temperatures and in the presence of methanol or triethanolamine as sacrificial agent (see supporting information, Figures S.11 and S.12). It was found that $H_2$ production increases with the temperature in the range

from 40 to 60 °C, reaching a maximum of 1200 μmol $H_2 \times g^{-1}$ at 60 °C compared to the 680 μmol $H_2 \times g^{-1}$ at ambient temperature. Further temperature increases to 65 or 70 °C results in a remarkable decrease in the $H_2$ production efficiency. This behavior can be rationalized considering a more favorable pore diffusion and activation of the dark steps up to 60 °C that would be overcompensated by an unfavorable electron-hole recombination at higher temperatures.

Tertiary amines have lower oxidation potential than alcohols and, therefore, this could be reflected in a higher $H_2$ production using triethanolamine as compared to methanol when the oxidation potential of the hole is close to that required to oxidize alcohols. In the present case, the initial rates of $H_2$ production are almost coincident for methanol and triethanolamine, although at long irradiation times, $H_2$ production using triethanolamine at 4 h was 780 μmol $H_2 \times g^{-1}$, higher than 680 μmol $H_2 \times g^{-1}$ achieved for methanol at the same irradiation time.

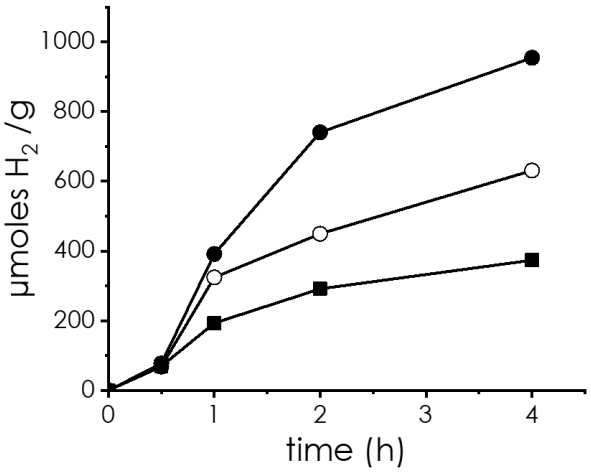


**Fig. 4.** Temporal profiles of hydrogen evolution using as photocatalyst (N)$C_\alpha$-2 upon irradiation with: ●UV-Vis ❍simulated sunlight irradiation and ■visible light (λ>420 nm).

To determine the wavelength region of the photons responsible for the photocatalytic activity of (N)$C_\alpha$-2, the $H_2$ evolution rates in the presence of methanol as sacrificial electron donor upon irradiation with UV-Vis, simulated sunlight and visible light (λ>450 nm) were compared. The

results are presented in Figure 4. As it can be observed there, part of the photocatalytic activity derives from the visible region. However, the minor percentage of UV and violet light present in simulated sunlight is highly efficient in $H_2$ generation. Moreover, (N)C$_\alpha$-2 even shows a notable $H_2$ productivity of about 30 % of the UV-Vis response upon irradiation at wavelengths longer than 520 nm (Figure S13). This photoresponse is in accordance with the optical bandgap determined for (N)C from the UV-Vis absorption spectra that is about 2.0 eV for (N)C$_\alpha$-2, as determined by the Tauc plot (see Table 1 and Figs., S14-S18 in Supporting information).

Occurrence of photoinduced charge separation and generation of electrons and holes was ascertained by performing metal photodeposition, monitoring the presence of metals by TEM imaging. Upon UV-Vis irradiation of a solution of $K_2PtCl_6$ in $H_2O$ containing methanol in the presence of (N)C$_\alpha$-2 as photocatalyst, formation of Pt nanoparticles of average particle size about 1-2 nm, characterized by its characteristic 111 interplanar distance of 0.224 nm, was observed. Figure 5 presents selected TEM images of the photodeposited Pt nanoparticles. Figure S19 in supporting information shows EDX analysis of the sample confirming Pt as the element of the nanoparticles.

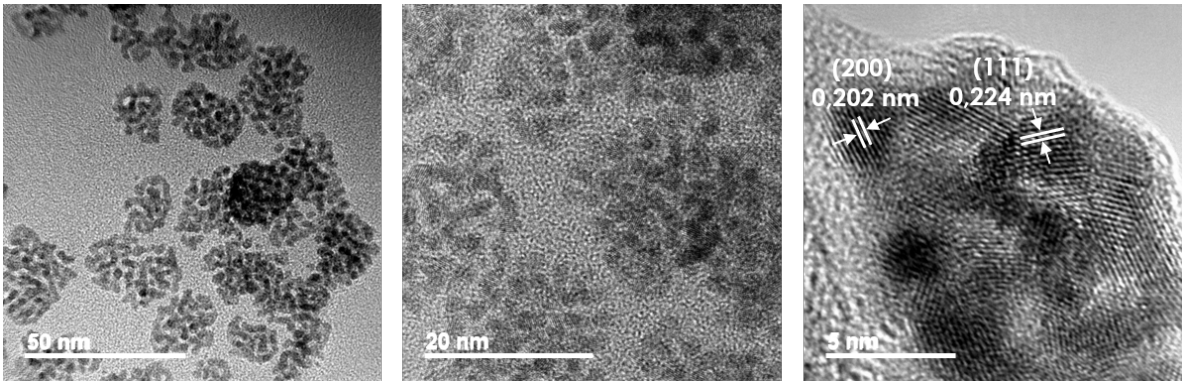


**Fig. 5.** HRTEM images taken in transmission mode of (N)C$_\alpha$-2 after irradiation in the presence of $H_2PtCl_6$, where the formation of small Pt nanoparticles can be clearly observed.

Interestingly, when using as photocatalyst, for $H_2$ generation in the presence of methanol, the (N)C$_\alpha$-2 material containing the photodeposited Pt nanoparticles, some increase in the $H_2$

evolution at long irradiation times from 650 $\mu mol \times g^{-1}$ in the absence of Pt to 790 $\mu mol \times g^{-1}$ in its presence was measured (see supporting information, Figure S.20). Pt is among the most common noble metals used as co-catalyst favoring $H_2$ evolution in semiconductors.[19] Remarkable increases in the $H_2$ evolution rate in semiconductors upon photodeposition of Pt of over one order of magnitude have been frequently observed.[20] Therefore, the minor influence of Pt on the photocatalytic activity of (N)$C_\alpha$-2 indicates that for this material, $H_2$ evolution is not kinetically a highly demanding process.

In fact, generally, oxygen evolution involving four electrons oxidation and four protons removal from two water molecules is the rate limiting process in overall water splitting. In the present case, (N)$C_\alpha$-2 as photocatalyst and using $Ag^+$ as electron acceptor was able to promote $O_2$ evolution and the reaction is accelerated after photodeposition of $CrO_2$. Figures S21 and S22 in the supporting information show TEM images of (N)$C_\alpha$-2 after photodeposition of $CrO_2$ and the corresponding EDS analysis confirming Cr as the element of the nanoparticles. Figure 6 presents the temporal $O_2$ evolution profiles. Estimation of the oxidation potential of valence band holes based

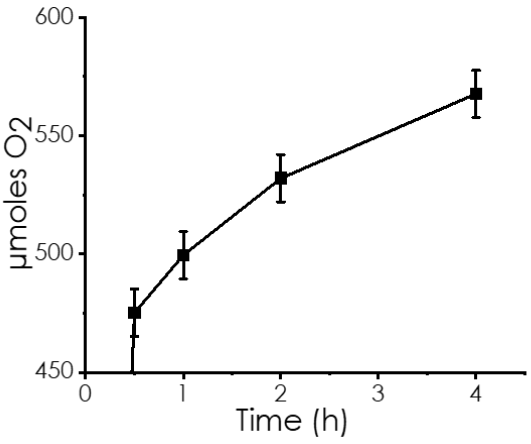


**Fig. 6.** Temporal oxygen evolution profile with (N)$C_\alpha$-2 in the presence of $CrO_2$ and Ag.

on the energy onset for electron detection in XPS, indicates that photogenerated (N)$C_\alpha$-2 holes should have an oxidation potential value of 1.33 V vs. NHE that should be sufficient for the 0.82 V required for oxygen evolution in neutral $H_2O$ plus an overpotential.

As indicated in the Introduction, the main purpose of the present study is to show how the conduction and valence band energy values of microporous graphitic carbons can be altered by N-doping. The energy of the upper edge of the valence band energy for samples (N)$C_\alpha$ was determined by XPS measuring the minimum energy required to detect the emission of electrons from the sample, corrected by the instrument work function. Supporting information provides a detailed information of these calculations. Bandgap, on the other hand, was determined from the Tauc plot of the absorption spectrum (Figures S14-S18). These measurements have allowed to determine the position of the conduction band minimum. The results are presented in Figure 7 in which for the position of conduction and valence bands of the undoped microporous graphitic carbons as well the standard potentials for $H_2$ and $O_2$ evolution from $H_2O$ at pH 7 have also included. As it can be seen there, N doping increases the energy of the valence band respect to the parent undoped graphitic carbon. This energy increase of valence band energy is gradual with the N content, (N)C-3 having a valence band energy insufficient to generate $O_2$ from $H_2O$. This tendency on the valence band energy can be interpreted considering that in the case of N doping, the lone electron pair on N atoms are contributing increasing to this state. The conduction band energy does not change much for (N)$C_\alpha$-1 and (N)$C_\alpha$-2 respect to the microporous graphitic carbon, except when N doping was excessive. Overall, (N)$C_\alpha$-1 and (N)$C_\alpha$-2 are well aligned to promote water splitting, even after considering and overpotential to increase the reaction rate. The narrower, well-aligned position of the bands for (N)$C_\alpha$-1 and (N)$C_\alpha$-2 can explain their higher photocatalytic activity compared to the parent, undoped microporous graphitic carbon.

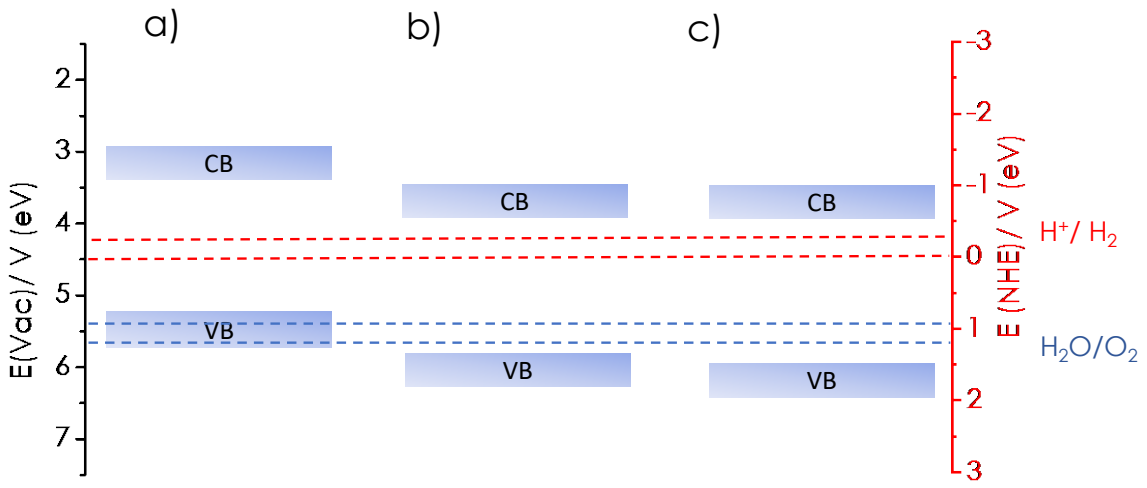


**Fig. 7.** Energy of the Valence Band (VB) Maximum and Conduction Band (CB) Minimum for the a) (N)$C_\alpha$-1, b) (N)$C_\alpha$-2 and c) (N)$C_\alpha$-3. Dotted lines correspond to the potentials of $H_2$ (red) and $O_2$ (blue) generation at pH 7 (higher values) or 0 (lower values)

We finally tested photocatalytic overall water splitting using (N)$C_\alpha$-2 as photocatalyst. Evolution of $H_2$ and $O_2$ upon UV-Vis irradiation of (N)$C_\alpha$-2 in pure $H_2O$ was observed, although, as expected in view of the much lower photocatalytic activity in the absence of sacrificial agents, the efficiency was lower affording 350 μmol $H_2 \times g^{-1}$ at 4 h UV-Vis irradiation and the corresponding stoichiometric amount of $O_2$. Figure 8 shows the temporal $H_2$ and $O_2$ evolution in these measurements.

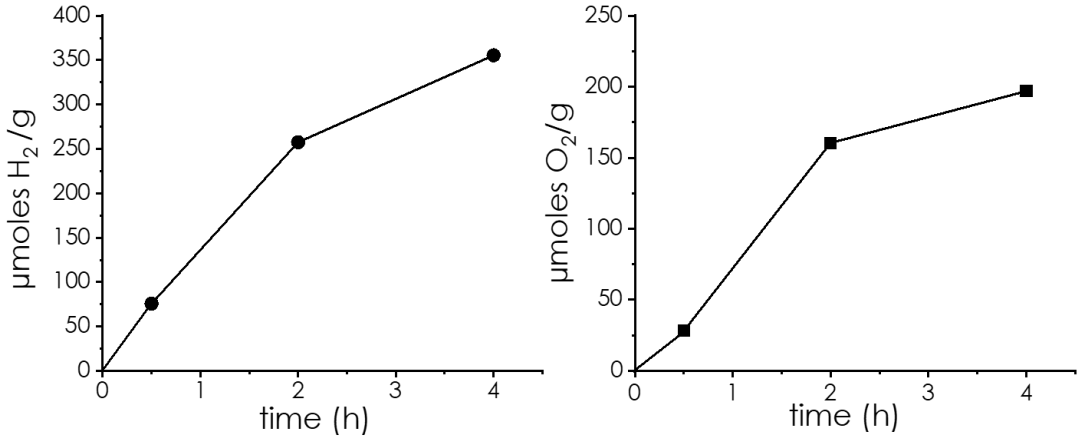


**Fig. 8.** Temporal evolution of ●$H_2$ and ■$O_2$ in µmols per total mass of photocatalyst (N)C$_\alpha$-2.

Photocurrent measurements confirm the occurrence of charge separation upon irradiation of (N)C. Electrodes were prepared by spreading a suspension of (N)C$_\alpha$-2 containing 1 wt % of Paraloid as a binder on transparent conductive FTO electrode. Cyclic voltammetry in 1 M KCl aqueous solution showed a weak reduction peak at about -200 mV vs. SCE that could be related to the presence of N or O atoms in the material, as well as the $H_2$ and $O_2$ evolution reactions with onsets at about -0.9 and 2.2 V vs. NHE, respectively. Irradiation with UV-Vis light of (N)C$_\alpha$-2 results in observation of a photocurrent that builds up under illumination and quickly disappears in the dark (see supporting information, Figures S.23-S.25). Photo action spectrum was recorded upon irradiation with monochromatic light. This photoresponse spectrum shows that besides in the UV region, (N)C$_\alpha$-2 has also a response band in the 470-625 nm zone in the visible region, this being in agreement with the previously observed photocatalytic activity under visible light irradiation.

## 4. Conclusions

The present results have shown how conduction and valence band alignment of microporous graphitic carbon derived from cyclodextrins can be engineered by N doping and how the position of these bands has a strong influence on the photocatalytic activity for overall water

splitting that is not observed for the parent graphitic carbons lacking N doping. There is an optimal N content for a maximum photocatalytic activity. Porosity has also an influence on the photocatalytic activity, the porous graphitic carbon derived from $\alpha$–cyclodextrin (pore dimensions 0.65 nm) exhibiting the highest $H_2$ production, reaching a productivity of 1.8 mmol $H_2 \times g^{-1}$ in 4 h that is a quite remarkable activity for a metal-free photocatalyst. These materials also exhibit activity under visible light ($\lambda$>420 nm) irradiation, even at wavelengths longer than 520 nm. Photoinduced generation of electrons and holes was ascertained by metal/metal oxide photodeposition and photocurrent measurements. Our study shows that the concept of band alignment by doping can be used to position the energy of the frontier orbitals of microporous graphitic carbons at the potentials required for the photocatalytic reaction, opening research to further increase the photocatalytic activity of carbon-based photocatalysts.

**Acknowledgements.**

Financial support by the Spanish Ministry of Science and Innovation (Severo Ochoa and CTQ2018-98237-CO2-1) and Generalitat Valenciana (Prometeo 2017-083) is gratefully acknowledged. AR and AP thanks the Spanish Ministry of Economy and Competitiveness for a postgraduate scholarship and a Ramon y Cajal research associate contract, respectively.

**References**

1. Niu, J.; Domenech-Carbó, A.; Primo, A.; Garcia, H.,Uniform nanoporous graphene sponge from natural polysaccharides as a metal-free electrocatalyst for hydrogen generation, *RSC advances* **2019,** *9*, 99-106.
2. Primo, A.; Atienzar, P.; Sanchez, E.; Delgado, J. M.; García, H.,From biomass wastes to large-area, high-quality, N-doped graphene: catalyst-free carbonization of chitosan coatings on arbitrary substrates, *Chemical communications* **2012,** *48*, 9254-9256.
3. He, J.; Anouar, A.; Primo, A.; García, H.,Quality Improvement of Few-Layers Defective Graphene from Biomass and Application for H2 Generation, *Nanomaterials* **2019,** *9*, 895.
4. Peng, Y.; Rendón-Patiño, A.; Franconetti, A.; Albero, J.; Primo, A.; Garcia, H.,Photocatalytic overall water splitting activity of templateless structured graphitic nanoparticles obtained from cyclodextrins, *ACS Applied Energy Materials* **2020**.

5. Rendón-Patiño, A.; Santiago-Portillo, A.; Vallés-Garcia, C.; Palomino, M.; Navalón, S.; Franconetti, A.; Primo, A.; Garcia, H.,Templateless Synthesis of Ultra-Microporous 3D Graphitic Carbon from Cyclodextrins and Their Use as Selective Catalyst for Oxygen Activation, *Small Methods* **2020,** *4*, 1900721.
6. Singh, R.; Bharti, N.; Madan, J.; Hiremath, S.,Characterization of cyclodextrin inclusion complexes—a review, *J. Pharm. Sci. Technol* **2010,** *2*, 171-183.
7. Li, Z.; Wang, M.; Wang, F.; Gu, Z.; Du, G.; Wu, J.; Chen, J.,γ-Cyclodextrin: a review on enzymatic production and applications, *Applied microbiology and biotechnology* **2007,** *77*, 245.
8. Kurkov, S. V.; Loftsson, T.,Cyclodextrins, *International journal of pharmaceutics* **2013,** *453*, 167-180.
9. Del Valle, E. M.,Cyclodextrins and their uses: a review, *Process biochemistry* **2004,** *39*, 1033-1046.
10. Rekharsky, M. V.; Inoue, Y.,Complexation thermodynamics of cyclodextrins, *Chemical reviews* **1998,** *98*, 1875-1918.
11. Corma, A.,From microporous to mesoporous molecular sieve materials and their use in catalysis, *Chemical reviews* **1997,** *97*, 2373-2420.
12. Martínez, C.; Corma, A.,Inorganic molecular sieves: Preparation, modification and industrial application in catalytic processes, *Coordination Chemistry Reviews* **2011,** *255*, 1558-1580.
13. Corma, A.; García, H.; Sastre, G.; Viruela, P. M.,Activation of Molecules in Confined Spaces: An Approach to Zeolite− Guest Supramolecular Systems, *The Journal of Physical Chemistry B* **1997,** *101*, 4575-4582.
14. Boronat, M.; Corma, A.,What is measured when measuring acidity in zeolites with probe molecules?, *ACS catalysis* **2019,** *9*, 1539-1548.
15. Primo, A.; Garcia, H.,Zeolites as catalysts in oil refining, *Chemical Society Reviews* **2014,** *43*, 7548-7561.
16. Lavorato, C.; Primo, A.; Molinari, R.; Garcia, H.,N-Doped Graphene Derived from Biomass as a Visible-Light Photocatalyst for Hydrogen Generation from Water/Methanol Mixtures, *Chemistry – A European Journal* **2014,** *20*, 187-194.
17. Eckmann, A.; Felten, A.; Mishchenko, A.; Britnell, L.; Krupke, R.; Novoselov, K. S.; Casiraghi, C.,Probing the nature of defects in graphene by Raman spectroscopy, *Nano letters* **2012,** *12*, 3925-3930.
18. Li, Z.; Lu, C.; Xia, Z.; Zhou, Y.; Luo, Z.,X-ray diffraction patterns of graphite and turbostratic carbon, *Carbon* **2007,** *45*, 1686-1695.
19. Yang, J.; Wang, D.; Han, H.; Li, C.,Roles of cocatalysts in photocatalysis and photoelectrocatalysis, *Accounts of chemical research* **2013,** *46*, 1900-1909.
20. Latorre-Sánchez, M.; Primo, A.; García, H.,P-doped graphene obtained by pyrolysis of modified alginate as a photocatalyst for hydrogen generation from water–methanol mixtures, *Angewandte Chemie International Edition* **2013,** *52*, 11813-11816.